



How electron tunneling and uphill excitation energy transfer support photochemistry in *Halomicronema hongdechloris*

Franz-Josef Schmitt¹ · Anne Hüls² · Marcus Moldenhauer² · Thomas Friedrich²

Received: 31 May 2023 / Accepted: 13 November 2023 / Published online: 10 January 2024
© The Author(s), under exclusive licence to Springer Nature B.V. 2023

Abstract

Halomicronema hongdechloris, the first cyanobacterium reported to produce the red-shifted chlorophyll *f* (Chl *f*) upon acclimation to far-red light, demonstrates remarkable adaptability to diverse light conditions. The photosystem II (PS II) of this organism undergoes reversible changes in its Chl *f* content, ranging from practically zero under white-light culture conditions to a Chl *f*: Chl *a* ratio of up to 1:8 when exposed to far-red light (FRL) of 720–730 nm for several days. Our ps time- and wavelength-resolved fluorescence data obtained after excitation of living *H. hongdechloris* cells indicate that the Soret band of a far-red (FR) chlorophyll involved in charge separation absorbs around 470 nm. At 10 K, the fluorescence decay at 715–720 nm is still fast with a time constant of 165 ps indicating an efficient electron tunneling process. There is efficient excitation energy transfer (EET) from 715–720 nm to 745 nm with the latter resulting from FR Chl *f*, which mainly functions as light-harvesting pigment upon adaptation to FRL. From there, excitation energy reaches the primary donor in the reaction center of PS II with an energetic uphill EET mechanism inducing charge transfer. The fluorescence data are well explained with a secondary donor P_{D1} represented by a red-shifted Chl *a* molecule with characteristic fluorescence around 715 nm and a more red-shifted FR Chl *f* with fluorescence around 725 nm as primary donor at the Chl_{D1} or P_{D2} position.

Keywords “Uphill” energy transfer · Electron transfer · Primary donor · Photosystem II · Electron tunneling · Far-red light · *Halomicronema hongdechloris* · Anti-Stokes luminescence

Introduction

Chlorophyll *f* (Chl *f*), the most red-shifted chlorophyll molecule known to date, was discovered in 2010 in the cyanobacterium *Halomicronema hongdechloris* (Chen et al. 2010, 2012). Chl *f* differs from Chl *a* by a formyl group present at the C-2 position, making it [2-formyl]-Chl *a* (Chen et al. 2010; Willows et al. 2013). Employment of red-shifted Chl species most likely reflects evolutionary adaption to the light conditions in the local environment (Chen et al. 2012; Ueno et al. 2019). This is well known for *Acaryochloris marina*, which is adapted to an ecological niche that is abundant in

far-red (FR) and near-infrared light, accumulating up to 99% of its total chlorophyll content as Chl *d* (Miyashita et al. 1996). This substitution of Chl *a* by Chl *d* in *A. marina*'s photosystems extends the spectrum of light that can be harnessed for oxygenic photosynthesis and carbon fixation by the organism to the near-infrared region (Mielke et al. 2011). Chl *d* mainly functions as a light-harvesting pigment in *A. marina* with an absorption maximum at 714–718 nm for PS II in living cells (Marquardt et al. 1997, Marquardt et al. 2000, Mimuro et al. 1999, Mimuro et al. 2000, Mimuro et al. 2004, Chen et al. 2005, Petrusek et al. 2005, Schmitt et al. 2006, Schmitt 2011, Theiss et al. 2011).

However, to this day, there is still a controversial debate about the nature of the primary and secondary donors in the PS II reaction center (RC) of *H. hongdechloris*. This accounts not only for the chemical nature, but also for the structural position of the involved chlorins, since recent studies discuss either Chl *a*, Chl *d*, or Chl *f* as possible candidates for the four central donor side chlorins in the PS II RC, which are P_{D1}, P_{D2}, Chl_{D1}, and Chl_{D2} (Nürnberg et al. 2018; Zamzam et al. 2020; Judd et al. 2020). It is

✉ Franz-Josef Schmitt
franz-josef.schmitt@physik.uni-halle.de

¹ Department of Physics, Martin-Luther-Universität Halle-Wittenberg, Von-Danckelmann-Platz 3, 06120 Halle (Saale), Germany

² Department of Bioenergetics, Institute of Chemistry PC 14, Technische Universität Berlin, Straße des 17. Juni 135, 10623 Berlin, Germany

proposed that the composition of PS II in *H. hongdechloris* is similar to *Chroococcidiopsis thermalis* which contains four Chl *f*, one Chl *d*, and about 30 Chl *a* molecules, while it seems to be clear that the primary donor is formed by a red-absorbing pigment with a maximum of the Q_y absorbance band at 726 nm (Zamzam et al. 2020; Judd et al. 2020). Zamzam et al. (2020) studied two different purified, isolated PS II core complexes. For the white-light (WL) measurements, these authors used *Thermosynechococcus elongatus*, whereas *Chroococcidiopsis thermalis* was used for the FRL measurements. Based on their results, Zamzam and coworkers established a model for the central reaction center, in which the pigments of the four Chl molecules (P_{D1} , P_{D2} , Chl_{D1} , and Chl_{D2}) and the two pheophytin molecules ($Pheo_{D1}$ and $Pheo_{D2}$) were varied to understand the changes induced by exposing the cells to FRL. However, it is still not finally clarified, which molecule at which position functions as the primary electron donor, but it was proposed that it is either Chl_{D1} or P_{D2} (Zamzam et al. 2020; Judd et al. 2020).

In the PS I reaction center, the primary donor is formed by FR Chl *d* in *A. marina* (Itoh et al. 2001, 2007; Tomo et al. 2008; Schenderlein et al. 2008). The nature of the primary donor of PS II in *A. marina* is most probably a Chl *a*/Chl *d* heterodimer as proven by the electrochromic shift introduced by a charged Chl *d* cation (Schlodder et al. 2007) or possibly a Chl *d* homodimer (Tomo et al. 2007). Therefore, the idea of functionally highly distinct and specialized heterodimers is appealing to understand the photochemistry in far-red light-absorbing species that possibly exhibit uphill excitation energy transfer (EET) mechanisms.

Red-shifted chlorophylls localized within the antenna system can work as energy traps retarding the EET to the reaction centers, thus, transiently storing energy for several nanoseconds. From such red-shifted traps EET occurs energetically uphill to finally induce charge separation in the reaction center. (Trissl 1993; Croce et al. 2000; Gobets and van Grondelle 2001; Jennings et al. 2003; Allakhverdiev et al. 2016). Such thermally activated EET from red states to bulk Chls was observed as a rate-limiting step for charge separation in the PS I from maize thylakoids (Croce et al. 2000). Direct evidence for uphill EET from red Chl to the special pair was observed in *Ostreobium* containing a large quantity of red Chl *a* molecules harvesting light above 700 nm (Wilhelm and Jakob 2006). A common technique for detecting uphill EET is the measurement of blue-shifted anti-Stokes fluorescence, which was demonstrated in chloroplasts with more than 100 nm wavelength shift after excitation with 800 nm (Hasegawa et al. 2011). In previous work on *H. hongdechloris*, we analyzed temperature-dependent anti-Stokes fluorescence and showed that EET can bridge an energy gap of up to 13 kJ mol⁻¹ according the Arrhenius-Eyring theory (Schmitt et al. 2019; Friedrich and Schmitt 2021).

Kurashov et al. showed that EET from red-shifted Chl *f* with an absorption maximum of up to 760 nm can reach the primary donor (most probably a Chl *a*/Chl *a'* heterodimer) in the PS I of *Synechococcus sp.* PCC 7335 (Kurashov et al. 2019), with a similar mechanisms also suggested for the PS I of *H. hongdechloris* (Kato et al. 2020).

Our former studies indicated that an entropy gain supports the EET from Chl *f* to the special pair in the PS II of *H. hongdechloris*, since only few Chl *f* molecules are coupled to a large pool of Chl *a* molecules, which might explain the efficient harvesting of red-shifted light at 745 nm. Such an entropy effect reduces the free energy gap between Chl *f* and Chl *a* during the endothermal EET process (Schmitt et al. 2019; Friedrich and Schmitt 2021).

H. hongdechloris seems to contain Chl *a*-containing and Chl *f*-containing PS II after FRL adaption (Schmitt et al. 2020), and the EET between phycobilisomes and the different PS II reaction centers is strongly remodeled after FRL acclimation (Schmitt et al. 2020). Due to the existence of PS II complexes containing either Chl *a* and Chl *f* or Chl *a* only, it can be assumed that the structure of at least one or two molecules of the secondary and possibly also of the primary donor at the P_{D1} , P_{D2} , and Chl_{D1} positions, respectively, is based on Chl *a* after FRL adaption—at least in a fraction of PS II reaction centers, and only one or two molecules are substituted by Chl *f* in some part of the reaction centers (Schmitt et al., 2020).

Zamzam et al. (2020) recently proposed that the secondary donor in the reaction center of PS II in *Chroococcidiopsis thermalis* might consist of red-shifted Chl *a* at the P_{D1} position while the primary donor is a FR chlorophyll at the Chl_{D1} position, which is either a Chl *d* or a Chl *f* (P720). This was concluded after observing an electrochromic shift of 21 ± 4 cm⁻¹ due to formation of the semiquinone anion, $Q_A^{\cdot-}$. From the wavelength (726 nm), it was concluded that the primary donor (PD) is a FR chlorophyll; however, the true chemical nature of the PD is still elusive. Judd et al. (2020) observed the same electrochromic shift and added that the PD might also be located at the P_{D2} position. We assume that the PS II of *Chroococcidiopsis thermalis* is possibly similar to *H. hongdechloris* but not necessarily identical as no evidence for Chl *d* in the PS II of *H. hongdechloris* was found so far.

Electron transfer between the Chl *a* and the FRL-absorbing chlorophyll takes place within a few picoseconds; therefore, EET occurs efficiently from P_{D1} to Chl_{D1} at room temperature. For our simulations, we set this value to 50 ps which is the time resolution limit of our instrumentation. According to Zamzam et al. (2020), the excited state of FRL-absorbing Chl *d*/Chl *f* (P720) at Chl_{D1} is energetically lower than Chl *a* in *Chroococcidiopsis thermalis*, and, presumably, there is no backward electron transfer possible to the Chl *a* at P_{D1} . The excited state is,

therefore, localized at P720. However, the authors showed that FRL-absorbing Chl *d*/Chl *f* not only occurs as a pigment in the antenna, but is directly involved in primary charge separation.

We propose that the localization of the excited state to P720 represents an optimum between the high-energy state of many Chl *a* molecules and the low-energy state of a few Chl *f* molecules. The picture is similar to an “uphill” EET supported by entropy, but it does not involve direct EET. More likely, it represents an energetic distribution of the electron wave function that gives rise to a charge separation from an energetically lower state, which in turn induces electron transfer (ET) into an energetically higher state. We follow this picture assuming that it is essential to bear in mind the fact that wave functions are extended, can overlap, and can give rise to electron tunneling processes to “overcome” or “penetrate” energetic barriers.

In such a sense, ET can occur via a Chl *a* in the P_{D1} position, where Chl *a* is practically involved as a supporting molecule with an energetic state between P680 and P720. The spectral position of the Chl *a* in the P_{D1} position is adjusted at the energetic optimum for efficient charge separation, ET to Pheo and subsequent stabilization by ET to Q_A.

Materials and methods

Cell culture

Halomicronema hongdechloris cultures were kept at room temperature (25 °C) in 50-mL Erlenmeyer flasks containing KES seawater medium under constant shaking, as described (Tomo et al. 2014; Chen et al. 2012) and were grown under far-red light (FRL) by illuminating culture flasks by a circular array of 720 nm LEDs. Far-red light intensity was adjusted to 10 $\mu\text{E m}^{-2} \text{s}^{-1}$, since at intensities exceeding this value, the cultures bleached rapidly, as described (Li et al. 2014). For reference, cells were grown under white light (WL) with an intensity of 30 $\mu\text{E m}^{-2} \text{s}^{-1}$. White light was obtained from “warm white natural neon tube” resembling a temperature spectrum of 3000 K (Osram, Munich, Germany).

Absorption spectra

Absorption spectra were recorded on methanolic total pigment extracts prepared from intact WL- or FRL-adapted *H. hongdechloris* filament bundles in a 1-cm quartz cuvette between 300 and 800 nm with a UV-1800 spectrophotometer (Shimadzu, Berlin, Germany) at room temperature (298 K).

Fluorescence emission a spectra

Fluorescence emission a spectra were recorded on intact *H. hongdechloris* filament bundles at room temperature in KES medium. For this purpose, cell colonies were placed directly in the middle of regular 1-cm quartz cuvettes with 1 mm optical path length. The cells were placed inside the excitation light beam and adjusted to maximize the fluorescence signal. The fluorescence and excitation spectra were measured with a Fluoromax-2 spectrofluorometer (Horiba Jobin Yvon, Bensheim, Germany). The cell filaments were excited at different wavelengths using a Xenon lamp (Osram XBO 100, Carl Zeiss, Germany) as light source and by wavelength selection with a monochromator, while emission spectra were recorded between 600 and 800 nm during excitation with 430 nm and 470 nm at room temperature. Slits were set to 4 nm for excitation and 4 nm for emission, while the integration time was 1 s and the increment 1 nm. Excitation spectra were recorded observing the fluorescence at 710 and 730 nm from 400 nm up to 10 nm below the corresponding observation wavelength.

Time- and wavelength-correlated single-photon counting (TWCSPC)

Spectrally resolved fluorescence decay curves were recorded on intact *H. hongdechloris* filament bundles at room temperature in KES medium. For this purpose, cell colonies were transferred into the ca. 1 mm diameter tip of a Pasteur pipette, which served as spectroscopic cuvette placed in the laser focus with a multi-axis translation stage. Measurements were performed employing a Hamamatsu R5900 16-channel multi-anode photomultiplier tube (PMT) with 16 separate output (anode) elements and a common cathode and dynode system (PML-16C, Becker&Hickl, Berlin, Germany) as described in (Schmitt et al. 2019). A 470 nm pulsed laser diode (LHD-470, Picoquant, Berlin) delivering 80 ps full-width at half-maximum (FWHM) pulses at a repetition rate of 20 MHz was used for excitation. The fluorescence was observed via a 488 nm longpass filter (AHF Analysentechnik, Tübingen, Germany).

Calculation of the decay-associated spectra (DAS) and decay-associated yield spectra (DAYS)

Decay associated spectra (DAS) were determined by fitting a theoretical model for the time-resolved fluorescence decay $F(t)$ for each measured wavelength section τ_i ($i = 1 \dots 16$). This model function is a multiexponential decay (up to four components) with individual amplitude prefactors $A_j(\tau_i)$ ($j = 1, \dots, 4$) for each measured wavelength section but common (global) fluorescence decay times τ_j ($j = 1, \dots, 4$) for the whole spectral range:

$$F(t, \tau_j, A_j(\lambda_i)) = \sum_{j=1}^4 A_j(\lambda_i) e^{-t/\tau_j} \quad (1)$$

As the measured data are a convolution of the system's instrumental response function, *IRF*, with the ideal data model the fit function *FIT* denotes to

$$FIT(t, \lambda_i, A_j(\lambda_i), \tau_j) = F_0(\lambda_i) + \int_0^\infty \left(IRF(t') \cdot \sum_{j=1}^4 A_j(\lambda_i) e^{-(t-t')/\tau_j} \right) dt' \quad (2)$$

The wavelength-dependent $A_j(\lambda_i)$ denote the amplitudes for the decay times τ_j ($j = 1, \dots, 4$). The fit procedure employing a Levenberg–Marquardt algorithm minimizing the reduced Chi square, $\chi_r^2(\lambda)$, for each wavelength channel after convolution of the fit function with the instrumental response function (IRF) is in detail described in (Schmitt 2011).

The result of this analysis is visualized by plotting $A_j(\tau_j)$ (see Eq. 2) for each lifetime τ_j which represents the DAS that reveal the spectral distribution of individual decay components. DAS can, therefore, provide information on different dynamic processes such as direct fluorescence decay of spectrally overlapping states and EET processes between coupled states.

The determination of the DAYS follows the DAS as described in detail in (Schmitt 2011) by multiplying the spectral shape of the fit amplitudes of all decay components in the DAS with the corresponding time constant of the decay component. In contrast to the DAS, the amplitudes represented in the DAYS are, therefore, proportional to the

overall signal amplitude (registered number of photons) that contributes to that component:

$$DAYS_j(\lambda) = \tau_j A_j(\lambda) \quad (3)$$

Mathematical modeling

The formalism of rate equations can be used treating different molecules as localized states. The solution of such linear rate equation systems allows to simulate the DAS assuming Gaussian emission from each fluorescent state (For details regarding the simulation, see Schmitt 2011; Schmitt et al. 2019).

Results and discussion

The absorption spectra of methanolic extracts from *H. hongdechloris* cells adapted to white light (WL) and far-red light (720 nm, FRL) for 3 days are shown in Fig. 1A after normalization to the same value in the Q_y absorption band of Chl *a* at 665 nm assuming that Chl *a* is the most stable (“invariant”) pigment over time compared to the other involved pigments (PBP and Chl *f*). The spectra reveal that there are distinct changes in pigment composition when *H. hongdechloris* cells were grown under FRL compared to the WL control sample (Fig. 1A, red vs. black curve). The difference between the absorption of FRL-adapted cells (red curve) and WL-adapted cells (black curve) is shown in Fig. 1B. After three days of FRL illumination, a distinct additional absorbance with maximum at 700–720 nm

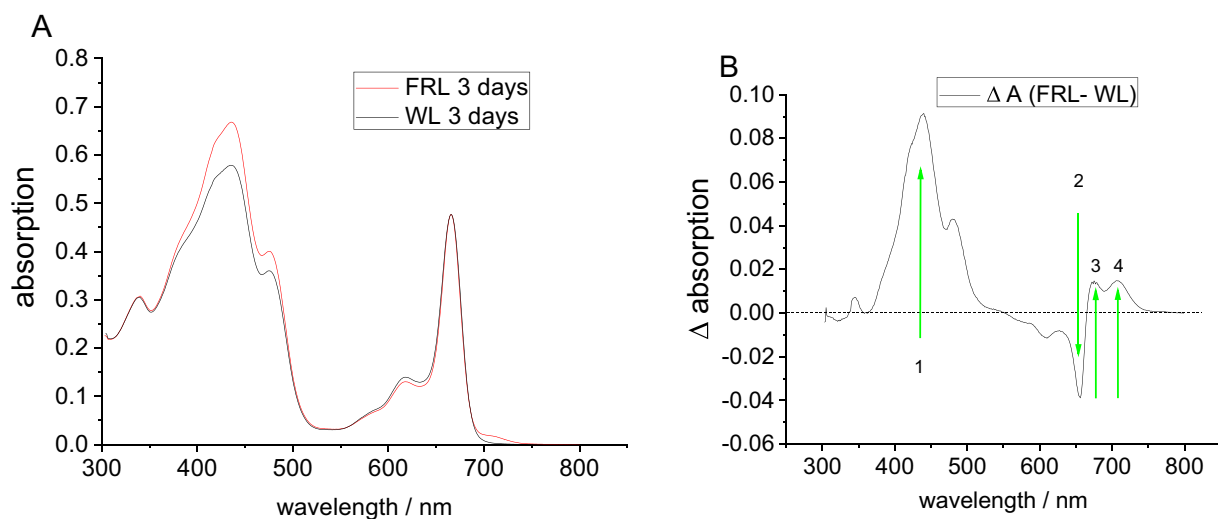


Fig. 1 **A** Room-temperature absorption spectra of methanolic extracts from *H. hongdechloris* cells adapted to WL (black line) and illuminated with FRL for three days (red line) after normalization

to the amplitude at 665 nm. **B** Difference absorbance spectra of *H. hongdechloris* extracts from FRL-adapted cells and the corresponding WL-adapted control sample as shown in panel (A)

appeared, which was absent in the WL-adapted samples, and is attributed to the formation of Chl *f* (see green arrow 4 in Fig. 1B) (Chen et al. 2010, 2012). The relative Chl *f* absorbance (determined as area of the Chl *f* absorption at 700–720 nm compared with a single Gaussian fit of the Q_y absorption band of Chl *a* at 665 nm) reaches up to 10% after 12 days of FRL illumination, but does not grow further (Schmitt et al. 2019). It is known that the Chl *a* content in FRL-adapted cells decreases so that the relative content of carotenoid absorption between 400–500 nm increases in FRL-adapted cells (see green arrow 1 in Fig. 1B) (Chen et al. 2012). In addition, a shift of the Q_y absorption band of Chl *a* is observed indicating that mainly the spectral contribution of blue-shifted Chls decreases (green arrow 2 in Fig. 1B) with an absorption maximum below 665 nm, while the content of red-shifted species with absorption at wavelengths larger than 665 nm increases (see green arrow 3 in Fig. 1B).

There is an absorption band in the range between 470 and 500 nm in both, WL- and FRL-adapted cells (Figs. 1, 2A, green arrow 1), which might correspond to the Soret band of a FR-absorbing Chl. The review of the absorption spectra of isolated PS I (Kurashov et al. 2019) and isolated PS II complexes (Judd et al. 2020; Zamzam et al. 2020) indicates, that this peak at 470 nm is mainly caused by pigments localized in photosystem II.

To further analyze the pigment composition, absorbance and fluorescence spectra of WL- and FRL-adapted samples after five days of FRL adaption are compared in Fig. 2. The fluorescence spectra are normalized to the amplitude at 686 nm as the Chl *a* emission is expected to be the most stable over time under all cultivation conditions. When put back to WL of an intensity of $30 \mu\text{E m}^{-2} \text{s}^{-1}$, the content of Chl *f* started to decline (Schmitt et al. 2019) indicating that Chl *f* formation in response to changes in the chromatic conditions is a reversible process. In addition, prominent changes due to

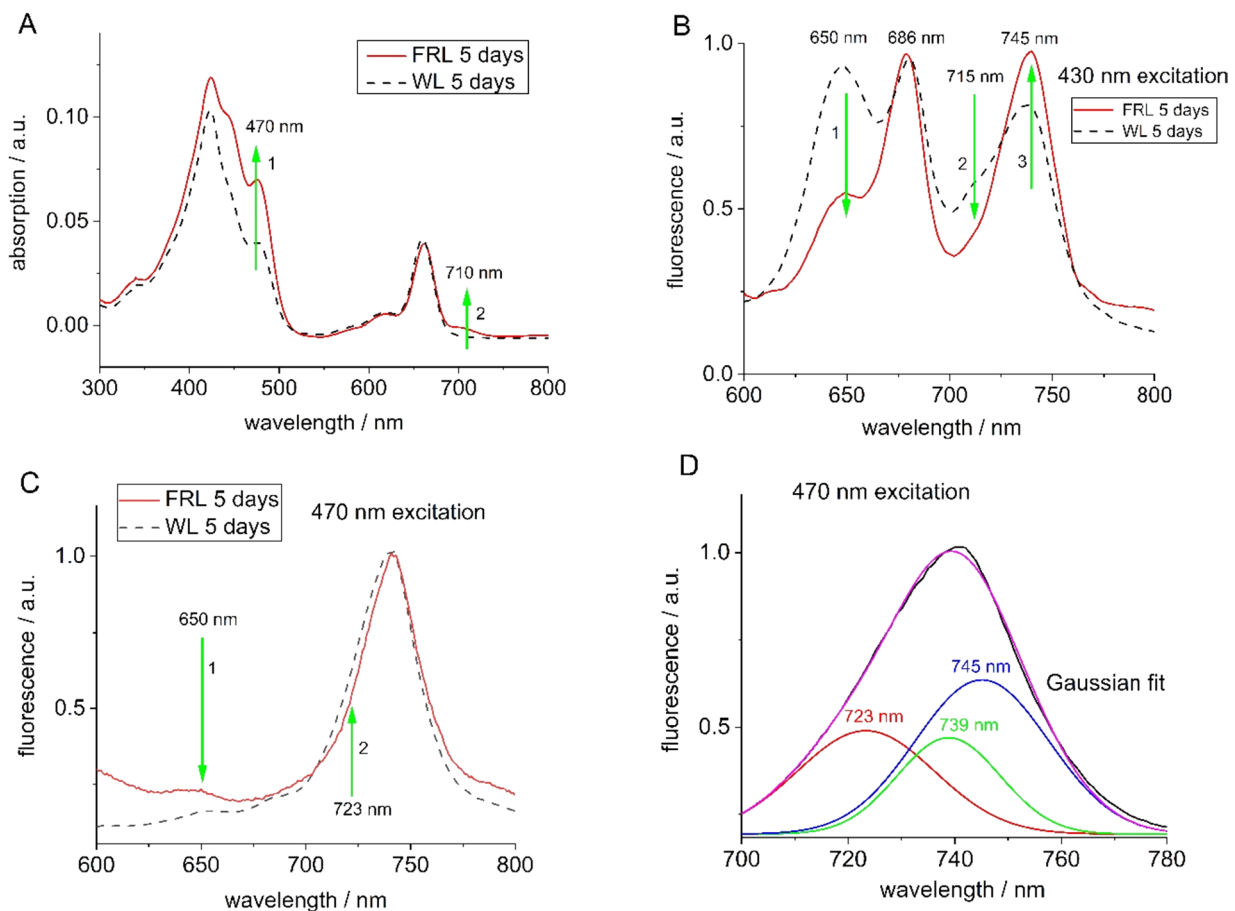


Fig. 2 **A** Room-temperature absorbance spectra of methanolic extracts of *H. hongdechloris* cells adapted to WL (dashed line) and cells adapted to FRL for 5 days (red solid line) normalized at 665 nm. **B** Room-temperature fluorescence emission spectra of intact WL-adapted *H. hongdechloris* cells upon excitation with 430 nm (dashed black curve) and samples adapted to FRL (red curve) for 5 days. **D** Fit of the fluorescence emission band from FRL-adapted cells as shown in (C) with three Gaussian bands between 700 and 800 nm

at 680 nm (reprinted with permission from Schmitt et al. 2020). **C** Room-temperature fluorescence emission spectra of intact WL-adapted *H. hongdechloris* cells upon excitation with 470 nm (dashed black curve) and samples adapted to FRL (red curve) for 5 days. **D** Fit of the fluorescence emission band from FRL-adapted cells as shown in (C) with three Gaussian bands between 700 and 800 nm

redistribution and remodeling of phycobilisomes (PBS) can be observed (Chen et al. 2012, 2010; Schmitt et al. 2020). However, since the bilin pigments are covalently attached to the phycobiliproteins (PBPs), they cannot be extracted by organic solvents, and, therefore, do not contribute to the spectral changes shown in Figs. 1 and 2A.

The absorbance of total methanolic pigment extracts from *H. hongdechloris* cells are shown in Fig. 2A after normalization at 665 nm. After 5 days of FRL adaption, more profound changes are observed between 400 and 500 nm due to increased carotenoid content (mainly β -carotene), as noted previously (Chen et al. 2012; Schmitt et al. 2019). This might be a mechanism to protect PS II, especially when reactive oxygen species (ROS) are formed (Schmitt et al. 2019, 2020). Carotenoids are efficient quenchers of ROS and of excited singlet and triplet states in PBS (Schmitt et al. 2014; Schmitt and Allakhverdiev 2017; Maksimov et al. 2014, 2015, 2016; Schmitt et al. 2020).

The absorbance spectrum of methanolic extracts of FRL-adapted *H. hongdechloris* cells (red solid line in Fig. 2A) exhibits a shoulder around 710 nm indicating Chl *f* production (green arrow 2 in Fig. 2A), which is visible after three days of FRL adaption (Fig. 1A) and reaches a maximum of about 10% compared to the Q_y peak of Chl *a* after 5–8 days. The Soret band of FR-absorbing Chls in PS II might be localized around 470 nm where a peak is visible in the absorption spectra (green arrow 1 in Fig. 2A). We, therefore, aimed to excite the chlorophylls via the Soret band at 430 nm to measure fluorescence and compare the results with fluorescence spectra observed after excitation at 470 nm (compare Fig. 2B and C).

Figure 2B shows the room-temperature fluorescence emission spectrum after excitation with 430 nm light. 430 nm light most probably excites both, Chl *a* and Chl *f*. The fit of Gaussian bands to the spectra as published previously (Friedrich and Schmitt 2021) reveals emission bands at 650 nm (PBS emission), 686 nm (Chl *a* emission), 715 nm, 739 nm, and 745 nm for FRL-adapted samples. The long-wavelength bands at 715 nm, 739 nm, and 745 nm might result from low-energy Chl *a* species, red-shifted PBS emission, and Chl *f* (Majumder et al. 2017; Tomo et al. 2014; Schmitt et al. 2019). The arrows in Fig. 2B indicate the reduction in fluorescence occurring at 650 nm due to the decay of PBPs during FRL adaption (green arrow 1 in Fig. 2B) for FRL-adapted cells, while fluorescence at 745 nm increases (green arrow 3 in Fig. 2B). Fluorescence at 715 nm is reduced after FRL adaption (green arrow 2 in Fig. 2B) indicating that it probably represents far-red PBPs or red-shifted Chl *a* species.

Strong reduction of the PBS content was observed in FRL-adapted cells indicating that PBSs degrade during FRL adaption down to the size of RL-absorbing APC cores (green arrow 1 in Fig. 2B) (Li et al. 2014, 2018).

Upon excitation with 470 nm (Fig. 2C, D), the peak at 650 nm is weak, in line with the low PBS absorption at 470 nm.

To disentangle the main emission at 740 nm occurring upon excitation with 470 nm, a Gaussian fit of the spectrum was carried out (Fig. 2D) to compare the results with the Gaussian fit of the fluorescence spectra measured upon excitation with 430 nm (Friedrich and Schmitt 2021). Interestingly, the fluorescence spectrum obtained upon excitation with 470 nm (Fig. 2C) indicates the presence of a Gaussian band at 723 ± 26 nm in form of a slight shoulder (see green arrow 2 in Fig. 2C and red curve in Fig. 2D) for both, WL- and FRL-adapted cells (dashed vs. red curve in Fig. 2C, D), which is not found in the spectrum obtained with 430 nm excitation.

The three Gaussian bands and their FWHM values are 723 ± 26 nm, 739 ± 19 nm, and 745 ± 25 (see Fig. 2D). The question arises, which emitter is responsible for the fluorescence around 723 nm that appears upon excitation with 470 nm in both WL- and FRL-adapted samples (region indicated by arrow 2 in Fig. 2C, red curve in Fig. 2D) but not after excitation with 430 nm.

To summarize the findings of the fluorescence study, there are at least four distinguishable long-wavelength emitters with remarkably different emission wavelengths of 715 nm (mainly observed upon 430 nm excitation) or 723 nm (mainly observed upon 470 nm excitation), 739 nm and 745 nm (with both, 430 nm and 470 nm excitation) occurring in the fluorescence spectra of FRL-adapted *H. hongdechloris* cells. The most red-shifted peaks at 739 nm and 745 nm are attributed to Chl *f* fluorescence, in line with previous observations (Chen et al. 2012; Schmitt et al. 2019). The presence of fluorescence in the 715–740 nm range in WL-adapted cells, in which no Chl *f* was detected (Chen et al. 2012), suggests that the emission contains contributions of far-red-shifted PBSs and red Chl *a* molecules already present in WL-adapted cells. Since the Soret band of Chl *a* is located at 430 nm, but shifts to the red in red-shifted Chl *a*, the transition from 715 nm upon 430 nm excitation to 725 nm upon 470 nm excitation indicates that there are distinguishable subspecies of Chl *a* or Chl *f* that exhibit Soret bands which shift from 430 to 470 nm.

The fluorescence excitation spectra of WL- and FRL-adapted cells of *H. hongdechloris* are shown in Fig. 3. It is clearly visible that far-red emission at 710 nm and 730 nm occurs in both, FRL- and WL-adapted cells (Fig. 3A, B red solid curves vs. dashed black curves). But there are different dependencies on the excitation wavelengths for the observed FRL emission in both cases.

In the WL-adapted samples, only a minor fraction of far-red fluorescence is excited via the Soret band of Chl *a* or Chl *f* (see green arrow 1 and 3, respectively, in Fig. 3A and B for the dashed curve). This accounts for both, 710 nm

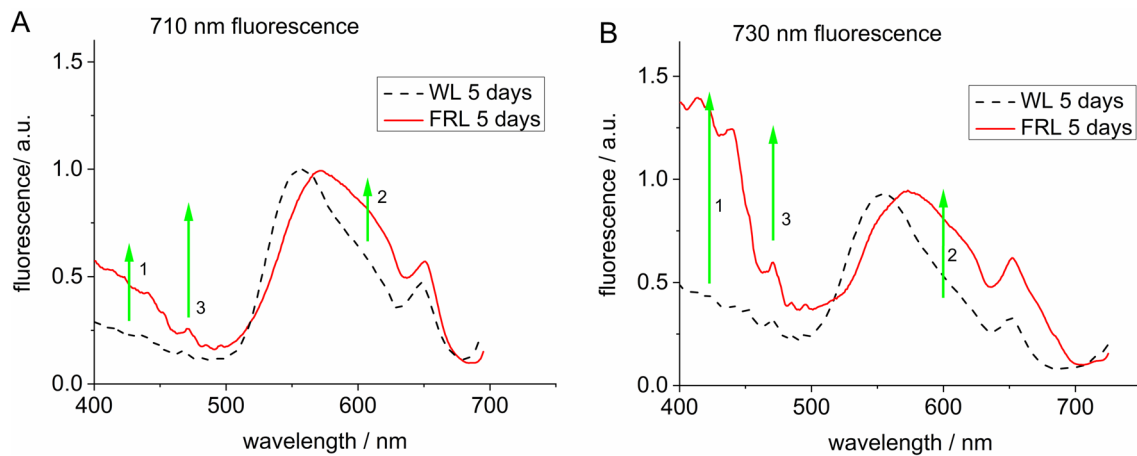


Fig. 3 Room-temperature fluorescence excitation spectra of *H. hongdechloris* cells adapted to WL (dashed black curves) and illuminated with FRL for five days (red curves), monitored at observation

(Fig. 3A) and 730 nm (Fig. 3B) fluorescence. In marked contrast, in FRL-adapted cells (red curves in Fig. 3), the 710 nm fluorescence (Fig. 3A), and especially the 730 nm fluorescence (Fig. 3B) is preferentially excited between 400 and 470 nm via the Chl Soret bands (see green arrow 1 and green arrow 3 in Fig. 3B): There is a small but characteristic peak at 470 nm, at which the Soret bands of red-shifted Chl *a* and Chl *f* might show stronger absorption (green arrow 3 in Fig. 3A and B). This indicates that especially the 730 nm fluorescence mainly results from FR chlorophylls, which might be red-shifted Chl *a* or Chl *f*. The 730 nm fluorescence is also directly excited via the Soret band of Chl *a* at 430 nm (indicating that Chl *a* is strongly coupled to the FR Chl). In Fig. 3, the difference between the dashed black curve and the red curve is more pronounced for the fluorescence emission at 730 nm as compared to 710 nm indicating that mainly the 730 nm emission is enhanced via specific emission channels formed due to FRL adaptation. In addition, for both, 710 nm emission and 730 nm emission, the absorption shifts to the red in FRL-adapted as compared to WL-adapted samples when excited via the PBSs (550–650 nm, green arrows 2 in Fig. 3A and B), which is in line with the finding that PBS degrade down to the long-wavelength-absorbing APC cores in FRL-adapted samples, which are responsible for the peak at 650 nm.

Overall, it is less likely to induce the red fluorescence at 710 nm by direct excitation into the Soret band of Chls. Rather, the 710 nm fluorescence is mainly excited via PBS absorption around 550 nm with an additional peak at 650 nm for APC, while fluorescence at 730 nm is more likely excited via the Soret bands of FR Chl *a* or Chl *f* in FRL-adapted samples (400–500 nm).

wavelengths 710 nm (A) and 730 nm (B). (Reprinted with permission from Friedrich and Schmitt 2021)

Time-resolved fluorescence spectra: DAS and DAYS at room temperature

Insights into processes such as excitation energy transfer (EET) and electron transfer (ET) can be obtained by correlating the time-resolved fluorescence in different spectral regions. Therefore, spectrally resolved fluorescence decays were recorded with 470 nm excitation (illumination intensity 100 W/m^2) on intact filament bundles of *H. hongdechloris* cells, either WL or FRL adapted for five days, using multi-channel TWCSPPC. The resulting decay-associated spectra (DAS) and decay-associated yield spectra (DAYS) of WL- and FRL-adapted samples are shown in Fig. 4.

All cells show a distinct spectral dependence of the 3 decay components (WL-adapted) or 4 decay components (FRL-adapted) used for fitting with the following time constants: A fast component of about 78 ps in WL-adapted samples (Fig. 4A,C) and two fast components with 40 ps (black squares) and 170 ps (red circles) in FRL-adapted samples (Fig. 4B,D), an intermediate component with 500 ps in WL- (red circles in Fig. 4A, C) and 710 ps in FRL-adapted samples (blue triangles in Fig. 4B, D), and a slow component with 1.1 ns in WL- (blue triangles in Fig. 4A, C) and 1.8 ns in FRL-adapted samples (green triangles in Fig. 4B, D). The DAYS show peaks and shoulders that can be attributed to the components at 650 nm (PBS emission), 686 nm (Chl *a* emission), and FR Chl *a* or Chl *f* in the long-wavelength regime at 710–725 nm and 740 nm (Fig. 4C, D), which had been determined by Gaussian fits of the fluorescence emission spectra (see Friedrich and Schmitt 2021, and Fig. 2D). In WL-adapted cells (Fig. 4A, C), the medium component (500 ps) peaks at 680 nm and at 740 nm, while the fast

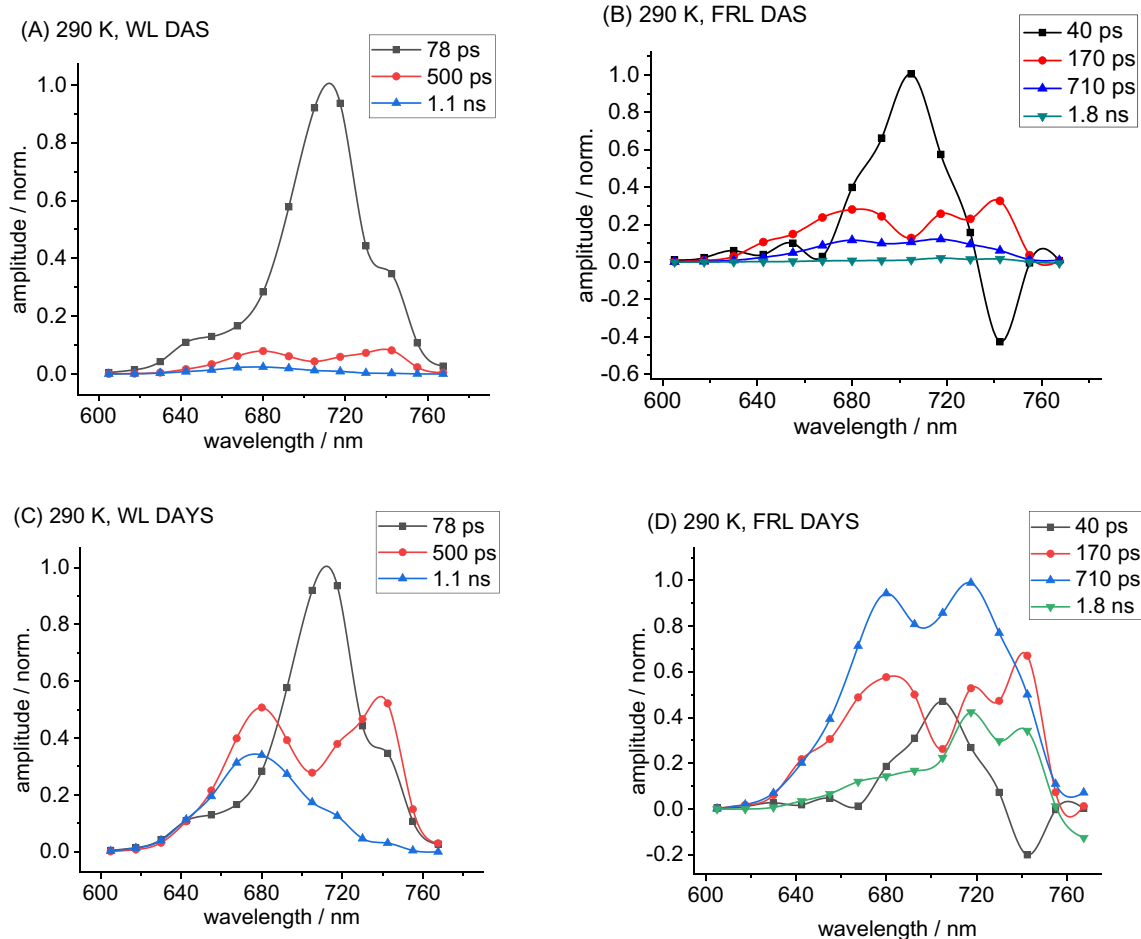


Fig. 4 Room-temperature decay-associated spectra (DAS) upon 470 nm excitation for WL- (A) or FRL-adapted cells (B) after global approximation by a sum of three exponential decay components for WL-adapted cells, and four components for FRL-adapted cells,

respectively. The decay-associated yield spectra (DAYS) were calculated according to Eq. 3 (see Materials and Methods) and are presented in (C) for WL-adapted and in (D) for FRL-adapted samples. FRL adaption was conducted for 5 days

78 ps component peaks around 715 nm (see especially the DAYS, Fig. 4C). This finding indicates that the fastest of the resolved EET/ET processes occur from a molecule emitting fluorescence at 715 nm, which is strongly excited with 470 nm. Therefore, we assume that this is a red-shifted Chl (most probably a far-red Chl *a*) absorbing at 470 nm, which is involved in charge separation.

In FRL-adapted cells (see DAS in Fig. 4B and DAYS in Fig. 4D), the fastest decay component of 40 ps (black squares) shows a peak at 700–710 nm and a distinct rise kinetics at 745 nm indicating a fast EET between the red-shifted Chl *a* and the most red-shifted Chl molecule(s), most probably a far-red Chl *f* at 745 nm. In addition, a long-wavelength component of 1.8 ns (green triangles in Fig. 4D) shows peaks at 720 nm and 745 nm indicating the presence of long-wavelength energy traps in the FRL-adapted samples. The intermediate time component is prolonged in FRL-adapted samples with 710 ps (blue triangles in Fig. 4B,

D) instead of 500 ps in WL-adapted samples (red circles in Fig. 4A, C) albeit with a similar spectral structure. Additionally, in FRL-adapted samples, the fast 170 ps component (red circles in Fig. 4B, D) shows peaks at 685 nm, 720 nm, and 745 nm indicating strong coupling between the corresponding states as they decay with the same time constant. The subsequent electron transfer (ET) from the primary donor and the charge stabilization upon electron transfer to the primary plastoquinone Q_A are found to be prolonged in FRL-adapted as compared to WL-adapted cells (Zamzam et al. 2020). The longest decay time constant of 1.1 ns results from (isolated) PBPs in WL-adapted samples at 650–680 nm (blue triangles, Fig. 4A, C), while a FR excitation energy trap with a time constant of 1.8 ns is formed in FRL-adapted samples at 720–740 nm (green triangles, Fig. 4B, D).

The DAS (Fig. 4A, B) and DAYS (Fig. 4C, D) show broad emission bands correlating to the different time constants, because the spectral components subsume several EET and

ET processes as well as contributions from PS I, which are difficult to disentangle because of the strong spectral overlap of all molecules. To overcome this limitation, we measured time-resolved fluorescence at low temperatures, in order to benefit from the reduced spectral overlap of the various species under these conditions.

DAS and DAYS at low temperatures

At low temperatures in WL-adapted cells (see DAS in Fig. 5A, C, E), four spectral regions of fluorescence emission can be discriminated. This is mainly visible in the DAYS at 10 K (Fig. 6E): The first is observed around 650 nm, which mainly comprises PBS fluorescence, the

DAS and DAYS at low temperatures

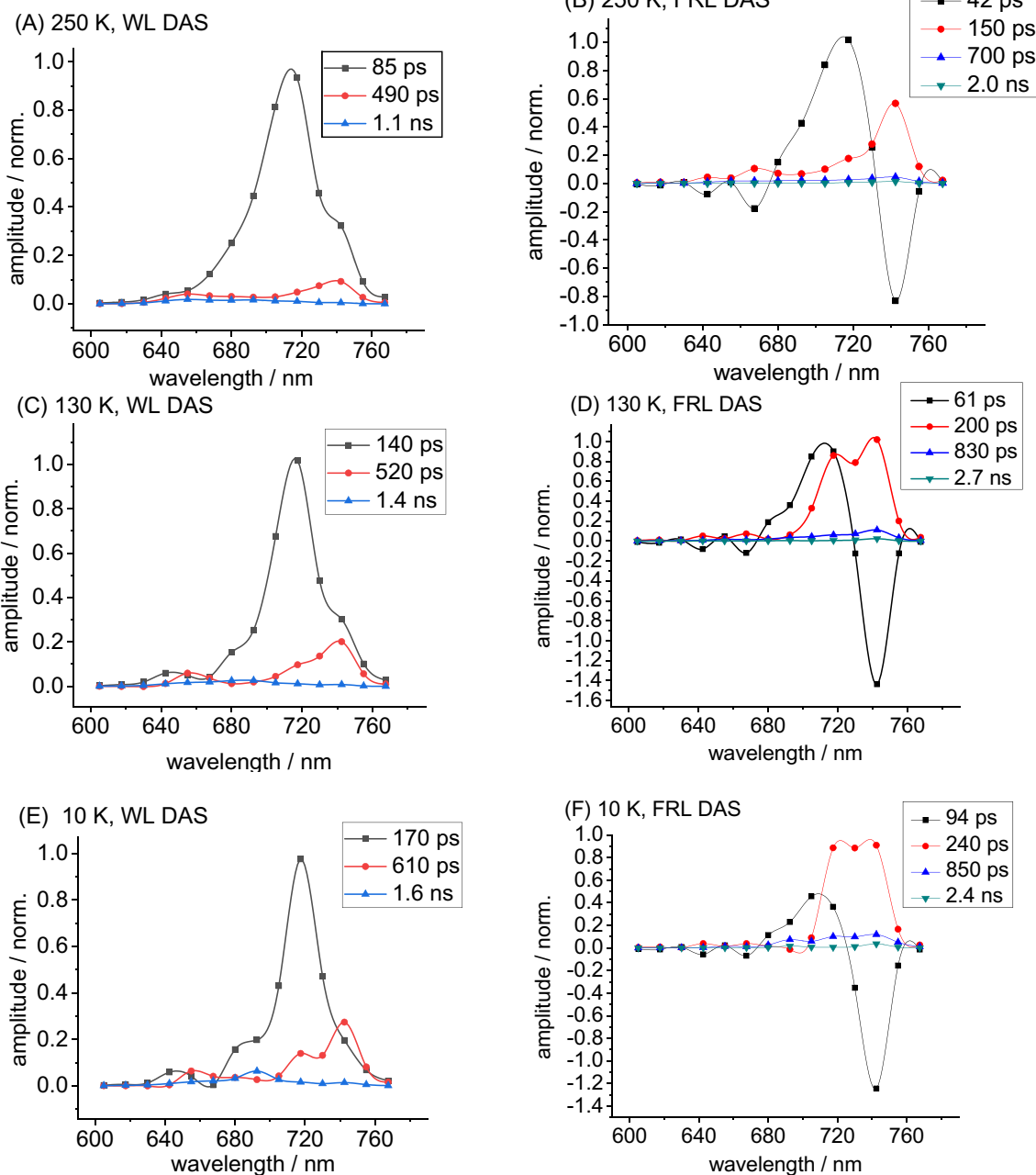


Fig. 5 Low-temperature DAS determined upon 470 nm excitation for WL- (left column, panels A, C, E) or FRL-adapted cells (right column, panels B, D, F) after global approximation of the fluorescence decay curves by a sum of three exponential components for WL-

adapted cells, and four components for FRL-adapted cells, respectively. The temperature varies between the figure panels from 250 K (A, B) over 130 K (C, D) to 10 K (E, F). FRL adaption was conducted for 5 days

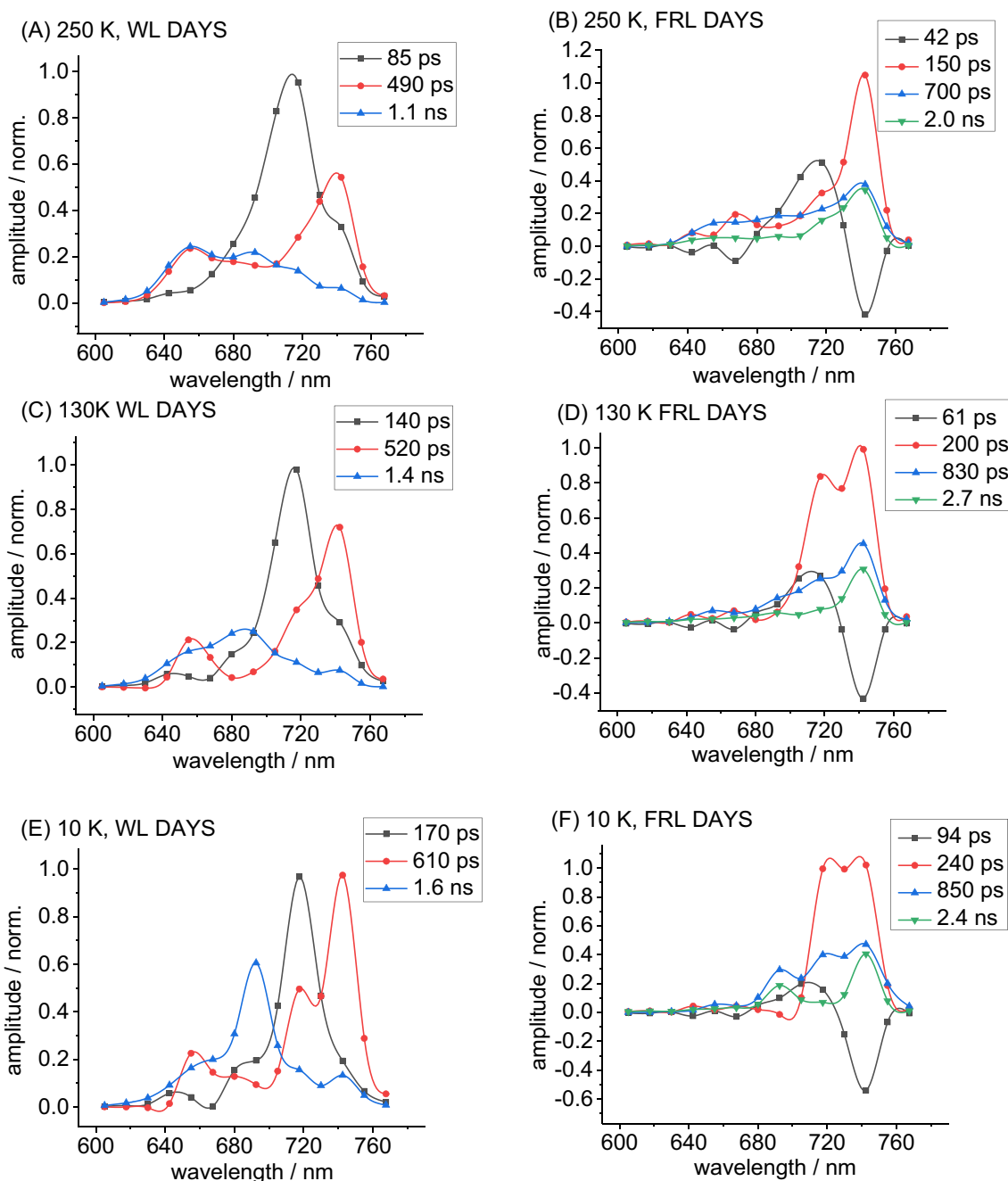


Fig. 6 Low-temperature decay-associated yield spectra (DAYS) determined upon 470 nm excitation for WL-(**A**, **C**, **E**) or FRL-adapted cells (**B**, **D**, **F**) by global approximation of the fluorescence decay curves with a sum of three exponential components for WL-

adapted cells, and four components for FRL-adapted cells, respectively. The temperature varies along the figure panels from 250 K (**A**, **B**) over 130 K (**C**, **D**) to 10 K (**E**, **F**). FRL adaption was conducted for 5 days

second is located around 686 nm, which can predominantly be attributed to Chl *a* (in PS II), the third is located around 720 nm, and, finally, the most red shifted is found around 740 nm. As discussed above, the band at 720 nm most probably results from red-shifted (FR) Chl, which could be Chl *a* or Chl *f* while the 740–745 nm peak results from FR Chl *f*.

In WL-adapted samples, we observed energetic decoupling of pigments upon cooling to very low temperatures (visible as rather isolated Gaussian bands of the different decay components as depicted in Fig. 6E), whereas in FRL-adapted cells, the emissions at 720 nm and 740 nm remain coupled (see blue, black and red curve in Fig. 6F). For the WL-adapted cells, three components are necessary

to obtain satisfactory fit results. The time constant of the fastest component (black squares) increases from 85 ps at 250 K (Fig. 5A) to 170 ps at 10 K (Fig. 5E), and it dominates the emission at 720 nm. The intermediate component (red circles) increases from 490 ps at 250 K (Fig. 5A) to 610 ps at 10 K (Fig. 5E). Both components dominate the DAS (Fig. 5) and DAYS (Fig. 6). In addition, a third component with a lifetime between 1.1 ns (250 K) and 1.6 ns (10 K) is found in WL-adapted samples (blue triangles in Fig. 5A, C, E), which contributes to both, the PBS (650 nm) and the Chl *a* regime (686 nm). In the DAS, the contribution of these components at 650 nm and 686 nm is hardly visible, since the excitation of PBSs and Chl *a* is low at 470 nm. In the DAYS, it can be seen that both, Chl *a* and PBSs, slightly emit with both time constants (470–600 ps, red circles and 1.1–1.6 ns, blue triangles). The long fluorescence lifetimes and the isolated peaks indicate that the PBSs and Chl *a*, which are partially excited at 470 nm, are not functionally coupled to the reaction center, and decay with slow time constants, which are typical for distorted isolated PBSs (Li et al. 2001; Schmitt et al. 2006; Schmitt 2010). The reason for the decoupling at low temperatures (10 K) might be due to slow freezing with a cooling rate of 1 K/s, which typically leads to PBS decoupling (Schmitt et al. 2006; Schmitt 2010; Schmitt et al. 2011; Schmitt et al. 2020; Maksimov et al. 2013). Interestingly, the red states at 720 nm and 740 nm decay fast even at the lowest temperature. The time constants at 10 K are determined as 170 ps (black squares, 720 nm) and 610 ps (red circles, 740 nm) (see Fig. 6E).

For FRL-adapted cells, satisfactory fits of the time-resolved fluorescence data are only obtained with four components, which were determined as 42 ps (250 K) to 90 ps (10 K) (black squares), 150 ps (250 K) to 240 ps (10 K) (red circles), 700 ps (250 K) to 850 ps (10 K) (blue triangles), and 2.0 ns (250 K) to 2.7 ns (130 K) (green triangles) (Fig. 5B, D, F and Fig. 6B, D, F).

The PBS fluorescence at 650 nm is almost abolished, in accordance with the fact that the PBS are degraded to APC cores upon FRL adaption, and hence, do not absorb at 470 nm. Also, at 685 nm, the emission is weaker compared to WL-adapted samples, and probably difficult to resolve due to the small amplitude. Thus, both fast components (black and red curves) again dominate the emission at 720 nm and 740 nm with a peak of the 40 ps (250 K, Fig. 6B) to 90 ps (10 K, Fig. 6F) (black squares) component in the region of 700–720 nm and the red curve 150 ps (250 K, Fig. 6B) to 240 ps (10 K, Fig. 6F) (red circles) peaking at 740 nm. However, there is a distinct difference between WL- and FRL-adapted cells, as the fastest component (black squares) shows a profound rise kinetics at 740 nm indicating a fast EET from 720 to 740 nm, which is responsible for the very fast time constant of the 40 ps (250 K, Fig. 6B) to 90 ps (10 K, Fig. 6F) component (black squares). In addition, the

second fastest component 150 (250 K, Fig. 6B) to 240 ps (10 K, Fig. 6F) (red circles) exhibits positive maxima both at 720 nm and 740 nm indicating that the emission of the two species occurs from a coupled system that spreads from 720 to 740 nm and involves both emitters, the putative primary donor at 720 nm and the far-red Chl *f* at 740 nm. We have to note that the spectral resolution of the DAS and DAYS is limited to about 12.5 nm, and, therefore, an exact determination of the wavelength ranges (as it is possible from absorption and fluorescence spectra) is not possible in the DAS and DAYS.

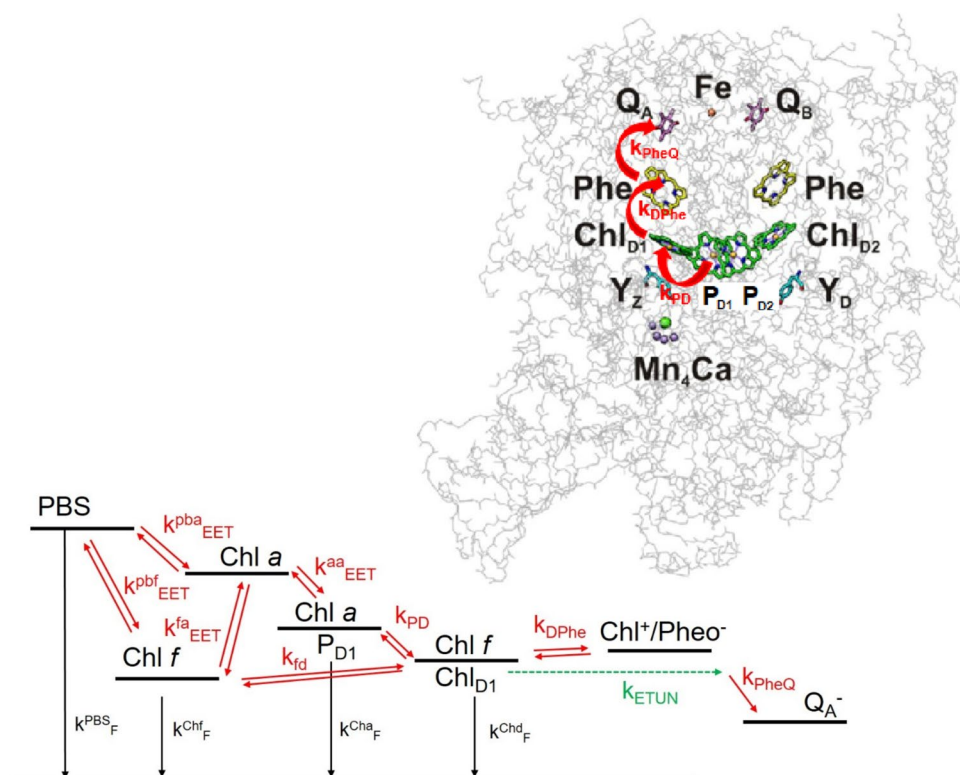
In order to interpret the DAS of WL- and FRL-adapted *H. hongdechloris* cells, we modeled the DAS by setting up a reaction scheme, which is structurally depicted in Fig. 7 based on the suggestion of Zamzam et al. (2020). This model represents a minimal kinetic scheme to explain the experimental observations. The DAS were all recorded upon excitation with 470 nm, assuming an excitation into the Soret band of red-shifted Chl *a* or Chl *f* species. Therefore, our simulation was performed assuming mainly excitation energy transfer (EET) and electron transfer (ET) processes from the red antenna molecules and the primary donor in the RC of PS II. The ET from the primary donor results in primary charge separation and the production of a radical pair consisting of the Chl⁺ cation and a pheophytin (in the following denoted as Chl⁺/Pheo⁻), from which the electron is then transferred further, and charge separation is stabilized by transfer to the primary plastoquinone Q_A (see Fig. 7).

Basically, two mechanisms contribute to the electron transfer (ET) processes in the course of charge separation: The first is thermally activated ET with a probability given by the Boltzmann factor $e^{-\frac{\Delta E}{kT}}$, and the second is caused by electron tunneling (ETUN), which is temperature-independent, and remains as the only ET mechanism at the lowest temperature (10 K), when the probability for thermally activated ET is zero.

To obtain further insights into the mechanism of EET, thermally activated ET, and ETUN processes at low temperatures, the logarithm of the fastest rate constant found in WL-adapted samples and of the second fastest rate constant in FRL-adapted samples was plotted against the reciprocal temperature in the form of Arrhenius graphs, which indicate thermally activated temperature regimes (linear rise of $\ln k$ with $1/T$) and the contribution of electron tunneling as a constant, i.e., temperature-independent, rate constant.

For the analysis of the temperature dependence of the rate constants according to the Arrhenius-Eyring theory, the fastest rate constant was chosen for WL-adapted cells, since these samples exhibit no significant EET between the excited species at deep temperatures. Therefore, it is assumed that this rate constant represents the ET from the primary donor. In FRL-adapted samples, one further decay component was necessary to fit the data satisfactorily, and the fastest

Fig. 7 Excitation energy and electron transfer scheme (reprinted with modification with permission from Mamedov et al. 2015). In the 3D structure of the PS II core complex, the redox cofactors are shown within the protein backbone: P_{D1} and P_{D2} denote the Chls of the reaction center; Chl_{D1} , Chl_{D2} , chlorophyll molecules on D1 and D2 proteins; Phe, pheophytin, one on D1 and another on D2; Q_A (on D2), a one-electron acceptor plastoquinone; Q_B (on D1), a two-electron acceptor plastoquinone. Red arrows indicate transfer processes with rate constants indicated. The kinetic scheme shows the rate constants involved in EET and ET processes occurring in the PS II reaction center of *H. hongdechloris* as used in the simulations



component (see black curve in Fig. 5B, D, F and Fig. 6B, D, F) exhibits a negative amplitude at 740 nm, which indicates fast EET to $Chl f$. Therefore, it is assumed that the second fastest time constant (red curves) represents ET from the primary donor in the FRL-adapted species. However, it can be seen that the qualitative temperature dependence is anyway similar for both rate constants (Fig. 8).

As can be inferred from Fig. 8A, the Arrhenius plot is a fairly linear function just for sufficiently high temperatures between 290 K ($1/T=0.0034$) and 130 K ($1/T=0.0077$), while for lower temperatures, the rate constant stays essentially constant. In this low-temperature regime, a temperature-independent electron tunneling process is apparently observed.

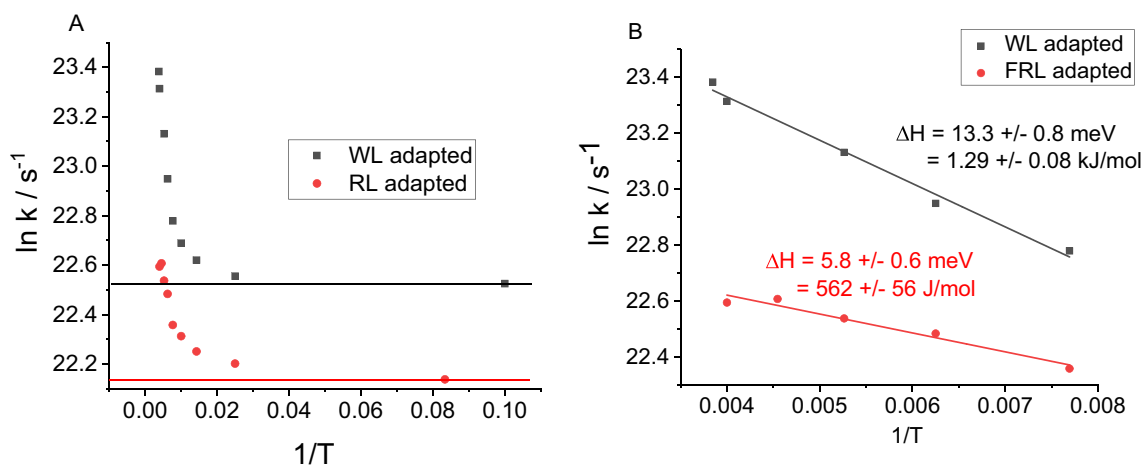


Fig. 8 **A** Arrhenius plots of the rate constant of fastest fluorescence component in WL-adapted samples (170 ps decay time at 10 K), and of the second fastest decay component in FRL-adapted samples (240 ps decay time at 10 K). **B** Expanded view of the thermally

activated temperature range from (A), fits of the negative slopes of the $\ln k$ values over $1/T$ are shown with resulting activation energies determined from the fitting results

For a quantitative analysis, an extended function was derived that includes both, thermally activated ET as well as electron tunneling (ETUN). In the most simple assumption, we anticipate that the overall rate constant for the electron transfer $k_{ges} = k(T) + k_0$ is composed of the sum of a temperature-dependent term $k(T)$ according the Arrhenius-Eyring theory, and a temperature-independent term k_0 , which represents ETUN as described by Eq. (4):

$$k_{ges} = k(T) + k_0$$

$$\tau_{ET} = \frac{1}{k_{ges}} = \frac{1}{k(T) + k_0} \tag{4}$$

Therefore, the natural logarithm of the overall rate constant for the ET, $k_{ges} = k(T) + k_0$, is a transcendental function for the temperature-dependent ET part that contributes to overcome the free energy ΔG according to $k(T) = A_0 \cdot \exp\left(\frac{-\Delta G}{k_B T}\right)$ and the temperature-independent ETUN part k_0 :

$$\ln k_{ges} = \ln\left(A_0 \cdot \exp\left(\frac{-\Delta G}{k_B T}\right) + k_0\right) \tag{5}$$

For temperatures approaching 10 K, the temperature-dependent term from the Arrhenius-Eyring theory can be neglected, and the low-temperature approximation holds, since $\ln k_{ges}(10\text{ K}) \approx \ln(k_0)$. However, at sufficiently high temperatures, the temperature-dependent term $k(T)$ determines the ET, and the total kinetics follows the Arrhenius-Eyring expression:

$$k(T) = A_0 \cdot \exp\left(\frac{-\Delta G}{k_B T}\right)$$

With the Gibbs–Helmholtz equation $\Delta G = \Delta H - T\Delta S$, it follows:

$$k(T) = A_0 \cdot \exp\left(\frac{-(\Delta H - T\Delta S)}{k_B T}\right) = A_0 \cdot \exp\left(\frac{\Delta S}{k_B}\right) \cdot \exp\left(\frac{-\Delta H}{k_B T}\right)$$

$$\rightarrow \ln k(T) = \ln\left(A_0 \cdot \exp\left(\frac{\Delta S}{k_B}\right)\right) - \frac{\Delta H}{k_B T} \tag{6}$$

And with the defintion.

$$\ln\left(A_0 \cdot \exp\left(\frac{\Delta S}{k_B}\right)\right) := -V$$

$$\rightarrow \ln \frac{1}{k(T)} = \frac{\Delta H}{k_B T} + V$$

This can be simplified in such a way that the slope of $\ln k(T)$ over $1/T$ follows the enthalpy difference between reaction products and educts $\frac{\Delta H}{k_B}$, while the intersection with the y-axis is determined by the expression $V = \ln\left(A_0 \cdot \exp\left(\frac{\Delta S}{k_B}\right)\right)$, which comprises the entropy difference and an (unknown) normalization factor A_0 that has the character of an effective entropy parameter (involving different numbers of electron donor and electron acceptor molecules, similar to a degeneracy factor or the effective density of states).

The following results are obtained for WL-adapted samples:

$$k_0 = (170\text{ps})^{-1} \quad \Delta H = 13.3\text{ meV}$$

and for FRL-adapted samples:

$$k_0 = (240\text{ps})^{-1} \quad \Delta H = 5.8\text{ meV}$$

These results imply that charge separation at 10 K from the primary donor takes place with a 170 ps time constant in WL-adapted samples, and with 240 ps in FRL-adapted samples, and is due to electron tunneling mainly.

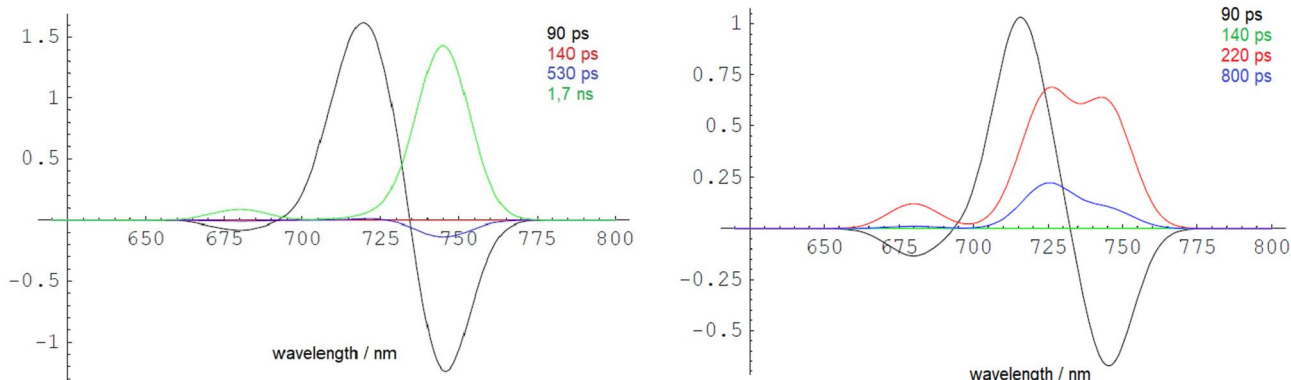


Fig. 9 Simulation of the DAS without ($k_{ETUN}=0$) (left side) and with electron tunneling ($k_{ETUN}=4\text{ ns}^{-1}$) (right side) for the EET and ET processes in FRL-adapted samples as depicted in Fig. 7 at 10 K.

The DAS on the right side reproduces the experimentally observed dynamics, as depicted in Fig. 5F

Simulation of the DAS

The DAS of the FRL-adapted *H. hongdechloris* cells at low temperatures (10 K) were simulated by developing a system of molecules with distinct excited states involved in EET and ET processes. The population dynamics of these states were then modeled with a rate equation system (see Friedrich and Schmitt 2021) as shown in Fig. 9. It was assumed that the secondary donor (P_{D1}) in the reaction center of PS II in *H. hongdechloris* might consist of red-shifted Chl *a* at the P_{D1} position, while the primary donor is a FR Chl at the Chl_{D1} position, which is most probably a Chl *f* as depicted in Fig. 7. The corresponding simulations of WL- and FRL-adapted samples at room temperature can be found in Schmitt et al. (2019, 2020).

Since the DAS were all recorded upon excitation with 470 nm into the Soret band of the primary donor in PS II, these models mainly encompass the primary charge separation and radical pair formation ($Chl^+/Pheo^-$). From pheophytin, the electron is then transferred to the primary plastoquinone Q_A . In addition, the antenna complexes contain PBS and domains of Chl *a* and Chl *f*, which are coupled by EET (see Fig. 7) (for details see Friedrich and Schmitt 2021).

With the choice of the time constants as depicted in Table 1, the simulated DAS as shown in Fig. 9 were obtained. Negative signs at the index letters mark the backwards transfer rates. While Fig. 9 (left side) shows the simulation result without electron tunneling (ETUN), the right side of Fig. 9 includes a tunneling rate constant of 4 ns^{-1} (250 ps time constant), which is included as the optional electron tunneling pathway in Fig. 7 (green arrow with rate constant k_{ETUN}). Remarkably, the agreement between experimental and simulated DAS (compare Fig. 9, right side with Fig. 5F) is satisfactory after inclusion of the ETUN process.

The results show that even at 10 K, charge separation occurs within 200 ps (k_{DPhe}) with just about 10% recombination probability (2 ns) (k_{DPhe}), which is only slightly smaller than the one of open and active PS II RCs at room

temperature. The charge stabilization by ET to plastoquinone Q_A (k_{PheQ}) is assumed to occur within 670 ps to fit the experimental data. Thus, for FRL-adapted cells, EET from Chl *a* to the far-red Chl as primary donor and the subsequent charge separation is even possible at 10 K.

If the system is simulated without an ETUN process, the lowest electronically excited state at 740 nm would quickly be populated at 10 K and would slowly decay with the intrinsic lifetime (1.7 ns) according to the long fluorescence decay time (see Fig. 9, left side). However, such a long-lived energy trap is not observed in the cells at 10 K. Therefore, the fluorescence at 740 nm cannot be emitted from an isolated long-lived trap at low temperatures (10 K). It decays fast and overcomes the excited states in the trap via depopulation by electron tunneling.

Conclusion

To summarize, we identified a small absorption band at 470 nm in FRL-adapted *H. hongdechloris* cells, which we attribute to the Soret band of the a red-shifted Chl molecule that might be the primary donor of PS II. Most probably, this molecule is a red-shifted Chl *a* at the P_{D1} and/or FR Chl *f* either at the Chl_{D1} or P_{D2} position (Zamzam et al. 2020; Judd et al. 2020).

Of note, a recent cryo-EM study, which reported the structure of far-red light-adapted PS II from *Synechococcus* sp. PCC 7335 at 2.25 Å resolution (Gisriel et al. 2022) identified one Chl *d* molecule in the Chl_{D1} position while at the P_{D1} position, Chl *a* is preserved even under FRL illumination similar to our assignment for *H. hongdechloris* containing Chl *f* as FRL pigment. Four additional Chl *f* molecules are found in the core antenna which function as red energy traps contributing to FRL absorption in *Synechococcus* sp. PCC 7335. Actually, the true chemical nature of the two chlorophyll molecules at the Chl_{D1} and P_{D1} position are not yet fully clarified but also the findings of Gisriel et al. support the general hypothesis that the FR-absorbing Chl is located at Chl_{D1} . Further structural work is required to elucidate whether these positional assignments are universally valid across many FRL-acclimating species or whether species-specific differences in chromophore composition may have developed in evolution.

Time-resolved fluorescence dynamics measured upon excitation with 470 nm light at room temperature and down to cryogenic temperatures of 10 K suggest that the molecule, which absorbs at 470 nm, facilitates or undergoes a charge transfer proceeding with a time constant of 160 ps even at 10 K in WL-adapted *H. hongdechloris* cells. Charge transfer at such a low temperature is supported by an electron tunneling mechanism. Support of this hypothesis was provided from the Arrhenius analyses of the fast fluorescence

Table 1 Rate constants used in the simulation shown in Fig. 9

Rate constant	ns^{-1}	Rate constant	ns^{-1}
k_{EET}^{pba}	3.3	k_{-EET}^{fa}	3
k_{EET}^{aa}	6	k_{-EET}^{aa}	0
k_{EET}^{pbf}	3.3	k_{-EET}^{pbf}	0
k_{EET}^{fa}	1	k_{-EET}^{fd}	3
k_{EET}^{fd}	4	k_{DPhe}	0.5
k_{PD}	20	k_{F}^{PBS}	0.8
k_{DPhe}	5	k_{F}^{Chf}	0.5
k_{PheQ}	1.5	k_{F}^{Chd}	0.5
k_{-EET}^{pba}	0	k_{F}^{Cha}	0.5
k_{ETUN}	4		

component, which exhibited a temperature-dependent and an additional temperature-independent contribution for the overall ET rate constant. The latter, temperature-independent component is characterized by a time constant of 160 ps in WL-adapted samples. The situation is similar in WL- and FRL-adapted cells, with the main difference in FRL-adapted samples that a further EET process from 720 to 740 nm can be found. This indicates the existence of a long-wavelength energy trap in the antenna system that consists of Chl *f* and is well coupled to Chl *a* at the P_{D1} and/or FR Chl *f* at the Chl_{D1} or P_{D2} position even at low temperatures. As the Chl *f* is strongly coupled to the primary donor even at low temperatures, fast depopulation of the Chl *f* excited states via an electron tunneling mechanism is possible that is only slightly slower compared to WL-adapted samples and was determined to 240 ps in FRL-adapted cells at 10 K.

Comparing the results obtained on WL- and FRL-adapted *H. hongdechloris* cells, we found that the primary donor shows fluorescence at about 725 nm in FRL-adapted samples with a strong absorption of the Soret band at 470 nm. Our method does not allow for the exact determination of the chemical nature of the primary and secondary donors which still could be a red-shifted Chl *a* or FR Chl *f*; however, the model simulations agree with our measurements when performed according to the assignment of Zamzam et al. (2020), assuming that the secondary donor in the reaction center of PS II in *H. hongdechloris* might consist of a red-shifted Chl *a* at the P_{D1} position, while the primary donor is a FR Chl at the Chl_{D1} position, which is most probably Chl *f* as depicted in Fig. 7.

As demonstrated in our previous work (Schmitt et al. 2019), Chl *f* is not only present as a pigment in the antenna system of *H. hongdechloris*, but it is also involved in direct ET within the reaction center, as shown in Fig. 7. However, in terms of energetics, the position of the real primary donor is located at 725 nm fluorescence wavelength, inbetween Chl *a* (686 nm fluorescence) and a long-wavelength antenna Chl *f* (745 nm fluorescence). This also accounts for the secondary donor, which is most probably a red-shifted Chl *a* in the P_{D1} position with fluorescence at 715 nm.

In this regard, we can confirm the results of Zamzam et al. (2020), who proposed a model for the central reaction center, which under WL adaptation conditions consists of the four Chl *a* molecules (P_{D1}, P_{D2}, Chl_{D1}, and Chl_{D2}) and the two pheophytins (Pheo_{D1} and Pheo_{D2}).

Such a primary donor Chl_{D1} and secondary donor P_{D1} being energetically located between Chl *a* and Chl *f* would be able to optimize the uphill energy transfer due to its intermediate energetic position, since it is optimally activated from Chl *f* and still has enough energy for water splitting in accordance with an electron tunneling process that supports the ET. The primary donor should not be too low in energy because according to the Marcus theory, the ET is

most efficient when electron donor and electron acceptor are in resonance. Admittedly, the recombination probability would also be large then; however, this process is efficiently suppressed in photosynthesis by sufficiently fast ET to Q_A, charge stabilization, membrane dynamics, and plastoquinone mobility, which ultimately separate the charges and enable an efficient and directional electron transfer.

Acknowledgements The authors are grateful for support by the German Research Foundation (DFG) under Germany's Excellence Strategy—EXC 2008/1–390540038 (UniSysCat). Dr. Neslihan Tavraz and Monika Weiß are gratefully acknowledged for careful cultivation of *H. hongdechloris* cells.

Author contributions FJS and TF: Developed the research questions. FJS: Developed the research program. FJS: Set up the experimental design. FJS, AH and MM: conducted the experiments. FJS, AH and TF: Wrote the manuscript. FJS and AH: Prepared the figures. MM: Provided the samples. TF Provided the research facilities, all authors reviewed the manuscript.

Data availability Not applicable.

Declarations

Conflict of interest The authors do not have conflict of interest.

References

- Allakhverdiev SI, Kreslavski VD, Zharmukhamedov SK, Voloshin RA, Korolkova DV, Tomo T, Shen JR (2016) Chlorophylls d and f and their role in primary photosynthetic processes of cyanobacteria. *Biochemistry (mosc)* 81(3):201–212. <https://doi.org/10.1134/S0006297916030020>
- Chen M, Telfer A, Lin S, Pascal A, Larkum AW, Barber J, Blankenship RE (2005) The nature of the photosystem II reaction centre in the chlorophyll d-containing prokaryote, *Acaryochloris marina*. *Photochem Photobiol Sci* 4:1060–1064. <https://doi.org/10.1039/b507057k>
- Chen M, Schliep M, Willows RD, Cai ZL, Neilan BA, Scheer H (2010) A red-shifted chlorophyll. *Science* 329:1318–1319. <https://doi.org/10.1126/science.1191127>
- Chen M, Li Y, Birch D, Willows RD (2012) A cyanobacterium that contains chlorophyll f—a red-absorbing photopigment. *FEBS Lett* 586:3249–3254. <https://doi.org/10.1016/j.febslet.2012.06.045>
- Croce R, Cinque G, Holzwarth AR, Bassi R (2000) The Soret absorption properties of carotenoids and chlorophylls in antenna complexes of higher plants. *Photosynth Res* 64:221–231. <https://doi.org/10.1023/A:1006455230379>
- Friedrich T, Schmitt F-J (2021) Red-Shifted and Red Chlorophylls in Photosystems: Entropy as a Driving Force for Uphill Energy Transfer? In: Allakhverdiev S (ed) *Photosynthesis: Molecular Approaches to Solar Energy Conversion*. Springer, Cham, pp 247–275
- Gisriel CJ et al (2022) Structure of a monomeric photosystem II core complex from a cyanobacterium acclimated to far-red light reveals the functions of chlorophylls *d* and *f*. *J Biol Chem* 298(1):1–15. <https://doi.org/10.1016/j.jbc.2021.101424>
- Gobets B, van Grondelle R (2001) Energy transfer and trapping in photosystem I. *Biochim Biophys Acta* 1507:80–99. [https://doi.org/10.1016/s0005-2728\(01\)00203-1](https://doi.org/10.1016/s0005-2728(01)00203-1)

- Hasegawa M, Yoshida T, Yabuta M, Terazima M, Kumazaki S (2011) Anti-Stokes fluorescence spectra of chloroplasts in *Parachlorella kessleri* and maize at room temperature as characterized by near-infrared continuous-wave laser fluorescence microscopy and absorption microscopy. *J Phys Chem B* 115:4184–4194. <https://doi.org/10.1021/jp111306k>
- Ho MY, Niedzwiedzki DM, MacGregor-Chatwin C, Gerstenecker G, Hunter CN, Blankenship RE, Bryant DA (2020) Extensive remodeling of the photosynthetic apparatus alters energy transfer among photosynthetic complexes when cyanobacteria acclimate to far-red light. *Biochim Biophys Acta Bioenerg* 1861(4):148064
- Itoh S, Iwaki M, Ikegami I (2001) Modification of photosystem I reaction center by the extraction and exchange of chlorophylls and quinones. *Biochim Biophys Acta* 1507:115–138. [https://doi.org/10.1016/s0005-2728\(01\)00199-2](https://doi.org/10.1016/s0005-2728(01)00199-2)
- Itoh S, Mino H, Itoh K, Shigenaga T, Uzumaki T, Iwaki M (2007) Function of chlorophyll d in reaction centers of photosystems I and II of the oxygenic photosynthesis of *Acaryochloris marina*. *Biochemistry* 46:12473–12481. <https://doi.org/10.1021/bi7008085>
- Jennings RC, Zucchelli G, Croce R, Garlaschi FM (2003) The photochemical trapping rate from red spectral states in PSI-LHCI is determined by thermal activation of energy transfer to bulk chlorophylls. *Biochim Biophys Acta* 1557:91–98. [https://doi.org/10.1016/s0005-2728\(02\)00399-7](https://doi.org/10.1016/s0005-2728(02)00399-7)
- Judd M, Morton J, Nürnberg D, Fantuzzi A, Rutherford AW, Purchase R, Cox N, Krausz E (2020) The primary donor of far-red Photosystem II: ChlD1 or PD2? *Biochim Biophys Acta Bioenergetics* 1861(10):148248. <https://doi.org/10.1016/j.bbabi.2020.148248>
- Kato K, Shinoda T, Nagao R, Akimoto S, Suzuki T, Dohmae N, Chen M, Allakhverdiev SI, Shen JR, Akita F, Miyazaki N, Tomo T (2020) Structural basis for the adaptation and function of chlorophyll f in photosystem I. *Nat Commun* 11:238. <https://doi.org/10.1038/s41467-019-13898-5>
- Kurashov V, Ho MY, Shen G, Piedad K, Laremore TN, Bryant DA, Golbeck JH (2019) Energy transfer from chlorophyll f to the trapping center in naturally occurring and engineered Photosystem I complexes. *Photosynth Res* 141:151–163. <https://doi.org/10.1007/s11120-019-00616-x>
- Li Y, Zhang J, Xie J, Zhao J, Jiang J (2001) Temperature-induced decoupling of phycobilisomes from reaction centers. *Biochim Biophys Acta* 1504:229–234. [https://doi.org/10.1016/s0005-2728\(00\)00250-4](https://doi.org/10.1016/s0005-2728(00)00250-4)
- Li Y, Lin Y, Loughlin PC, Chen M (2014) Optimization and effects of different culture conditions on growth of *Halomicronema hongdechloris* - a filamentous cyanobacterium containing chlorophyll f. *Front Plant Sci* 5:67. <https://doi.org/10.3389/fpls.2014.00067>
- Li Y, Lin Y, Garvey CJ, Birch D, Corkery RW, Loughlin PC, Scheer H, Willows RD, Chen M (2016) Characterization of red-shifted phycobilisomes isolated from the chlorophyll f-containing cyanobacterium *Halomicronema hongdechloris*. *Biochim Biophys Acta* 1857:107–114. <https://doi.org/10.1016/j.bbabi.2015.10.009>
- Li Y, Vella N, Chen M (2018) Characterization of isolated photosystem I from *Halomicronema hongdechloris*, a chlorophyll f-producing cyanobacterium. *Photosynthetica* 56:306–315. <https://doi.org/10.1007/s11099-018-0776-x>
- Majumder EL, Wolf BM, Liu H, Berg RH, Timlin JA, Chen M, Blankenship RE (2017) Subcellular pigment distribution is altered under far-red light acclimation in cyanobacteria that contain chlorophyll f. *Photosynth Res* 134:183–192. <https://doi.org/10.1007/s11120-017-0428-1>
- Maksimov EG, Schmitt FJ, Hätti P, Klementiev KE, Paschenko VZ, Renger G, Rubin AB (2013) Anomalous temperature dependence of the fluorescence lifetime of phycobiliproteins. *Laser Phys Lett* 10(5):055602
- Maksimov EG, Schmitt FJ, Shirshin EA, Svirin MD, Elanskaya IV, Friedrich T, Fadeev VV, Paschenko VZ, Rubin AB (2014) The time course of non-photochemical quenching in phycobilisomes of *Synechocystis* sp. PCC6803 as revealed by picosecond time-resolved fluorimetry. *Biochim Biophys Acta Bioenerg* 1837(9):1540–1547. <https://doi.org/10.1016/j.bbabi.2014.01.010>
- Maksimov EG, Shirshin EA, Sluchanko NN, Zlenko DV, Parshina EY, Tsoraev GV, Klementiev KE, Budylin GS, Schmitt FJ, Friedrich T, Fadeev VV, Paschenko VZ, Rubin AB (2015) The signaling state of orange carotenoid protein. *Biophys J* 109(3):595–607. <https://doi.org/10.1016/j.bpj.2015.06.052>
- Maksimov EG, Moldenhauer M, Shirshin EA, Parshina EA, Sluchanko NN, Klementiev KE, Tsoraev GV, Tavraz NN, Willoweit M, Schmitt FJ, Breitenbach J, Sandmann G, Paschenko VZ, Friedrich T, Rubin AB (2016) A comparative study of three signaling forms of the orange carotenoid protein. *Photosynth Res* 130(1–3):389–401. <https://doi.org/10.1007/s11120-016-0272-8>
- Mamedov M, Govindjee NV, Semenov A (2015) Primary electron transfer processes in photosynthetic reaction centers from oxygenic organisms. *Photosynth Res* 125:51–63. <https://doi.org/10.1007/s11120-015-0088-y>
- Marquardt J, Senger H, Miyashita H, Miyachi S, Mörschel E (1997) Isolation and characterization of biliprotein aggregates from *Acaryochloris marina*, a prochloron-like prokaryote containing mainly chlorophyll d. *FEBS Lett* 410:428–432. [https://doi.org/10.1016/s0014-5793\(97\)00631-5](https://doi.org/10.1016/s0014-5793(97)00631-5)
- Marquardt J, Mörschel E, Rhiel E, Westermann M (2000) Ultrastructure of *Acaryochloris marina*, an oxyphotobacterium containing mainly chlorophyll d. *Arch Microbiol* 174:181–188. <https://doi.org/10.1007/s002030000194>
- Mielke SP, Kiang NY, Blankenship RE, Gunner MR, Mauzerall D (2011) Efficiency of photosynthesis in a Chl d-utilizing cyanobacterium is comparable to or higher than that in Chl a-utilizing oxygenic species. *Biochim Biophys Acta* 1807:1231–1236. <https://doi.org/10.1016/j.bbabi.2011.06.007>
- Mimuro M, Akimoto S, Yamazaki I, Miyashita H, Miyachi S (1999) Fluorescence properties of chlorophyll d-dominating prokaryotic alga, *Acaryochloris marina*: studies using time-resolved fluorescence spectroscopy on intact cells. *Biochim Biophys Acta* 1412:37–46. [https://doi.org/10.1016/s0005-2728\(99\)00048-1](https://doi.org/10.1016/s0005-2728(99)00048-1)
- Mimuro M, Hirayama K, Uezono K, Miyashita H, Miyachi S (2000) Uphill energy transfer in a chlorophyll d-dominating oxygenic photosynthetic prokaryote. *Acaryochloris Marina Biochim Biophys Acta* 1456:27–34. [https://doi.org/10.1016/s0005-2728\(99\)00095-x](https://doi.org/10.1016/s0005-2728(99)00095-x)
- Mimuro M, Akimoto S, Gotoh T, Yokono M, Akiyama M, Tsuchiya T, Miyashita H, Kobayashi M, Yamazaki I (2004) Identification of the primary electron donor in PS II of the Chl d-dominated cyanobacterium *Acaryochloris marina*. *FEBS Lett* 556:95–98. [https://doi.org/10.1016/s0014-5793\(03\)01383-8](https://doi.org/10.1016/s0014-5793(03)01383-8)
- Miyashita H, Ikemoto H, Kurano N, Adachi K, Chihara M, Miyachi S (1996) Chlorophyll d as a major pigment. *Nature* 383:402
- Nürnberg DJ, Morton J, Santabarbara S, Telfer A, Joliot P, Antonaru LA, Ruban AV, Cardona T, Krausz E, Boussac A, Fantuzzi A, Rutherford AW (2018) Photochemistry beyond the red limit in chlorophyll f-containing photosystems. *Science* 360(6394):1210–1213. <https://doi.org/10.1126/science.aar8313>
- Petrásek Z, Schmitt FJ, Theiss C, Hoyer J, Chen M, Larkum A, Eichler HJ, Kemnitz K, Eckert HJ (2005) Excitation energy transfer from phycobiliprotein to chlorophyll d in intact cells of *Acaryochloris marina* studied by time- and wavelength-resolved fluorescence spectroscopy. *Photochem Photobiol* 4:1016–1022. <https://doi.org/10.1039/b512350j>
- Schenderlein M, Çetin M, Barber J, Telfer A, Schlodder E (2008) Spectroscopic studies of the chlorophyll d containing photosystem I

- from the cyanobacterium, *Acaryochloris marina*. *Biochim Biophys Acta, Bioenergetics* 1777:1400–1408. <https://doi.org/10.1016/j.bbabo.2008.08.008>
- Schlodder E, Cetin M, Eckert HJ, Schmitt FJ, Barber J, Telfer A (2007) Both chlorophylls a and d are essential for the photochemistry in photosystem II of the cyanobacteria. *Acaryochloris Marina Biochim Biophys Acta* 1767:589–595. <https://doi.org/10.1016/j.bbabo.2007.02.018>
- Schmitt F-J (2010) Temperature induced conformational changes in hybrid complexes formed from CdSe/ZnS nanocrystals and the phycobiliprotein antenna of *Acaryochloris marina*. *J Opt* 1:084008. <https://doi.org/10.1088/2040-8986/12/8/084008>
- Schmitt F-J (2011). Picobiophotonics for the investigation of pigment-pigment and pigment-protein interaction in photosynthetic complexes. PhD Thesis, TU Berlin (2011). <http://opus4.kobv.de/opus4-tuberlin/frontdoor/index/index/docId/3012>
- Schmitt F-J, Allakhverdiev SI (2017). *Reactive Oxygen Species: Signaling Between Hierarchical Levels in Plants*. John Wiley & Sons (2017). ISBN: 978-1-119-18488
- Schmitt F-J, Theiss C, Wache K, Fuesers J, Andree S, Handoyo A, Karradt A, Kiekebusch D, Eichler HJ, Eckert H-J (2006) Investigation of the excited states dynamics in the Chl d-containing cyanobacterium *Acaryochloris marina* by time- and wavelength correlated single-photon counting. *Proc SPIE* 6386:638607. <https://doi.org/10.1117/12.689127>
- Schmitt FJ, Maksimov EG, Suedmeyer H, Jeyasangar V, Theiss C, Paschenko VZ, Eichler HJ, Renger G (2011) Time resolved temperature switchable excitation energy transfer processes between CdSe/ZnS nanocrystals and phycobiliprotein antenna from *Acaryochloris marina*. *Phot Nanostruct-Fundamentals Appl* 9(2):190–195
- Schmitt F-J, Kreslavski VD, Zharmukhamedov SK, Friedrich T, Renger G, Los DA, Kuznetsov VV, Allakhverdiev SI (2014) The multiple roles of various reactive oxygen species (ROS) in photosynthetic organisms. In: Allakhverdiev SI (ed) *Photosynthesis: A New Approach to the Molecular, Cellular, and Organismal Levels*. Wiley, Hoboken. <https://doi.org/10.1002/9781119084150.ch1>
- Schmitt F-J, Campbell ZY, Bui MV, Hüls A, Tomo T, Chen M, Maksimov EG, Allakhverdiev SI, Friedrich T (2019) Photosynthesis supported by a chlorophyll f-dependent, entropy-driven uphill energy transfer in *Halomicronema hongdechloris* cells adapted to far-red light. *Photosynth Res* 139:185–201. <https://doi.org/10.1007/s11220-018-0556-2>
- Schmitt F-J, Campbell ZY, Moldenhauer M, Friedrich T (2020) Light-induced phycobilisome dynamics in *Halomicronema hongdechloris*. *J Photochem Photobiol a: Chem.* 403:112838. <https://doi.org/10.1016/j.jphotochem.2020.112838>
- Theiss C, Schmitt F-J, Pieper J, Nganou C, Grehn M, Vitali M, Olliges R, Eichler HJ, Eckert HJ (2011) Excitation energy transfer in intact cells and in the phycobiliprotein antennae of the chlorophyll d containing cyanobacterium *Acaryochloris marina*. *J Plant Physiol* 168:1473–1487. <https://doi.org/10.1016/j.jplph.2011.02.002>
- Tomo T, Okubo T, Akimoto S, Yokono M, Miyashita H, Tsuchiya T, Noguchi T, Mimuro M (2007) Identification of the special pair of photosystem II in a chlorophyll d-dominated cyanobacterium. *PNAS* 104(17):7283–7288. <https://doi.org/10.1073/pnas.0701847104>
- Tomo T, Kato Y, Suzuki T, Akimoto S, Okubo T, Noguchi T, Hasegawa K, Tsuchiya T, Tanaka K, Fukuya M, Dohmae N, Watanabe T, Mimuro M (2008) Characterization of highly purified photosystem I complexes from the chlorophyll d-dominated cyanobacterium *Acaryochloris marina* MBIC 11017. *J Biol Chem* 283:18198–18209. <https://doi.org/10.1074/jbc.M801805200>
- Tomo T, Shinoda T, Chen M, Allakhverdiev SI, Akimoto S (2014) Energy transfer processes in chlorophyll f-containing cyanobacteria using time-resolved fluorescence spectroscopy on intact cells. *Biochim Biophys Acta* 1837:1484–1489. <https://doi.org/10.1016/j.bbabo.2014.04.009>
- Trissl HW (1993) Long-wavelength absorbing antenna pigments and heterogeneous absorption bands concentrate excitons and increase absorption cross-section. *Photosynth Res* 35(3):247–263. <https://doi.org/10.1007/bf00016556>
- Ueno Y, Aikawa S, Kondo A, Akimoto S (2019) Adaptation of light-harvesting functions of unicellular green algae to different light qualities. *Photosynth Res* 139:145–154. <https://doi.org/10.1007/s11220-018-0523-y>
- Wilhelm C, Jakob T (2006) Uphill energy transfer from long-wavelength absorbing chlorophylls to PS II in *Ostreobium* sp. is functional in carbon assimilation. *Photosynth Res* 87:323–329. <https://doi.org/10.1007/bf00016556>
- Willows RD, Li Y, Scheer H, Chen M (2013) Structure of chlorophyll f. *Org Lett* 15:1588–1590. <https://doi.org/10.1021/ol400327j>
- Zamzam N, Rakowski R, Kaucikas M, Dorlhiac G, Viola S, Nürnberg DJ, Fantuzzi A, Rutherford AW, van Thor JJ (2020) Femtosecond visible transient absorption spectroscopy of chlorophyll-f-containing photosystem II. *Proc Natl Acad Sci U S A* 117(37):23158–23164. <https://doi.org/10.1073/pnas.2006016117>

Publisher's Note Springer Nature remains neutral with regard to jurisdictional claims in published maps and institutional affiliations.

Springer Nature or its licensor (e.g. a society or other partner) holds exclusive rights to this article under a publishing agreement with the author(s) or other rightsholder(s); author self-archiving of the accepted manuscript version of this article is solely governed by the terms of such publishing agreement and applicable law.